Available online at www.sciencedirect.com
ScienceDirect
Physics Procedia 5 (2010) 483–493
Physics Procedia
www.elsevier.com/locate/procedia

LANE 2010

Novel fusion welding technology of glass using ultrashort pulse lasers

Isamu Miyamoto[a,b*], Kristian Cvecek[c], Yasuhiro Okamoto[e], Michael Schmidt[c,d]

[a] *Osaka Universitu, 2-1 Yamada-Oka, Suita, Osaka 565-0871, Japan*
[b] *Erlangen Graduate School of Advanced Optical Technolies (SAOT), Paul-Gordon Str. 6, 91052 Erlangen, Germany*
[c] *Bayerisches Laserzentrum, Konrad-Zuse Str. 2-6, 91052 Erlangen, Germany*
[d] *Lehrstuhl für Photonische Technologien, Paul-Gordan-Str. 3, 91052 Erlangen, Germany*
[d] *Okayama University, Tsushimanaka 3-1-1, Okayama 700-8350, Japan*

Invited Paper

Abstract

A novel fusion welding technology of glass using ultrashort laser pulses with high pulse repetition rates has been developed, where the laser energy is selectively absorbed at the interface by nonlinear process to provide crack-free welding without pre- and post-heating. A laser-matter interaction model is developed to evaluate the distribution of the ultrashort pulse laser energy absorbed in bulk glass. A thermal conduction equation is derived to calculate transient 3-dimensional temperature distribution and dimensions of molten zone in glass. The mechanical strength of weld joint is evaluated taking into consideration of the attracting force of the optical contact between the glass plates needed for keeping the high-temperature plasma in the bulk glass.

Keywords: Ultrashort pulse laser, nonlinear process, glass, thermal conduction, free eletron, temperature distribution, scrack

1. Introduction

First fusion welding of glass was reported using CW CO_2 laser where laser energy is deposited into 96%-silicate glass through vapor filled capillary called 'keyhole' [1]. This procedure has, however, drawbacks that whole thickness of the glass plate has to be melted in overlap welding due to opacity of the laser beam to the glass, and crack-free welding can be obtained only with glass plates having low thermal expansion coefficient.

Recently a novel fusion welding technology using ultrashort laser pulses of *fs* [2-4] and *ps* regime [5] with transparent wavelength, where laser energy is absorbed in bulk glass by nonlinear process, and crack-free welding is possible even in glass with large thermal expansion coefficient. The remarkable advantage of the process is only the interface of the glass plates can be melted locally without absorbent unlike the case of transmission welding of plastics [6]. Laser-matter interaction has not been, however, well understood, in spite of extensive study including evaluation of nonlinear absorptivity at *fs* [3] and *ps* pulses [5,7], thermal conduction analysis [5], joining dissimilar

*Corresponding author. Tel.: +81-798-47-1095; fax: +81-798-47-1095
E-mail address: isamu.miyamoto@ares.eonet.ne.jp

1875-3892
doi:10.1016/j.phpro.2010.08.171

glasses [8] and evaluation of mechanical strength of weld joint [8,9].

In this paper, the nonlinear absorptivity is experimentally evaluated using laser pulses of a duration of 10*ps* at wavelength of 1.064*nm*, and laser-matter interaction model is developed in fusion welding of glass using ultrashort laser pulses, which evaluates the distributions of the laser energy density absorbed in the plasma column and thereby the free electron density evolved in the internal melting of glass with ultrashort laser pulses at high repetition rates. An analytical equation is derived, by which the transient 3-dimensional temperature distributions in the plasma column is calculated. The mechanical strength of the melt region of bulk glass as well as weld joint is also evaluated.

2. Characteristics of internal melting of glass by ultrashort laser pulses

2.1. Nonlinear absorptivity

It has been shown that reflection and scattering of the laser energy by the laser-induced plasma are neglected in internal melting of glass by *ps* pulses [5,10]. Then the nonlinear absorptivity *A* of the glass sample is given by [5]

$$A = 1 - \frac{Q_t}{Q_0} \frac{1}{(1-R)^2} \tag{1}$$

where Q_0 is incident laser pulse energy, Q_t transmitted laser pulse energy and R Fresnel reflectivity. In this procedure, Q_t was determined by measuring the averaged laser power transmitted through the glass sample. The nonlinear absorptivity was evaluated at different translation speeds of the glass sample. **Figure 1(a)** shows the nonlinear absorptivity in different glass materials including borosilicate glass (Schott D263), Pyrex, Crown glass and quartz plotted vs. pulse energy at a pulse repetition rate of 640*kHz* focused by an objective lens of NA0.55. It is noted that little difference in the threshold pulse energy for the nonlinear absorption was observed despite of large difference in the band gap energy of the glass materials. The threshold energy was approximately 0.2μJ except for D263, which showed a little larger value. At large pulse energies, the material with larger band gap provided lower nonlinear absorptivity.

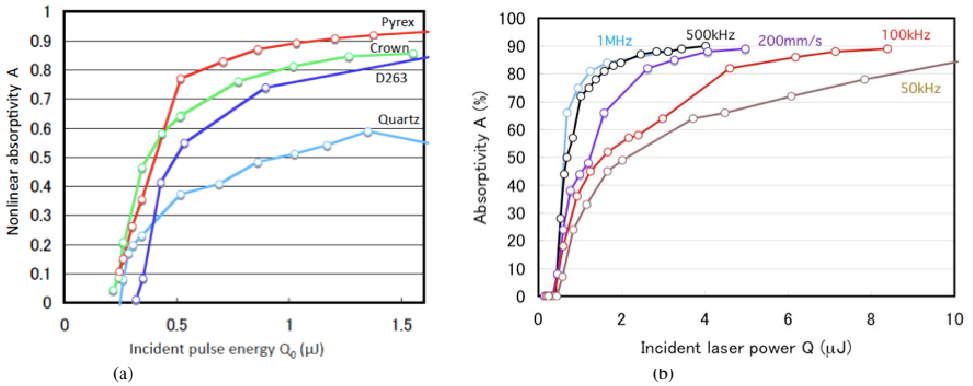

Fig. 1. Nonlinear absorptivity measured at *v*=20*mm/s* for (a) different glass materials at a pulse repetition rate of 640*kHz* and (b) different pulse repetition rates (D263). (wavelength *λ:* 1.064*μm*, pulse duration:10*ps*, NA0.55)

Figure 1(b) shows the nonlinear absorptivity measured at different pulse repetition rates in D263. It is seen that the nonlinear absorptivity increases with increasing pulse repetition rate at given pulse energy. This is because the temperature of the sample increases due to the heat accumulation at higher pulse repetition rates so that the number of thermally excited free electron to conduction band is increased, as is discussed latter on.

2.2. Shape and size of molten zone

Ultrashort laser pulses were irradiated in the bulk glass moving at a constant translation speed, and the cross-section of the glass sample was observed by a transmission-microscope. Typical cross-sections of D263 and fused silica are shown in **Fig. 2**, where the region of the transmission change shows ellipse or tear drop-shaped region. When two glass plates are welded in an overlap configuration, the interface disappeared in the region where the transmission changed (see Fig.11b). We regarded this region as '*melted*', although glass has no clear melting point. The cross-sectional area of D263 is approximately four times larger than fused silica due to lower melting temperature and thermal diffusivity (**Table 1**).

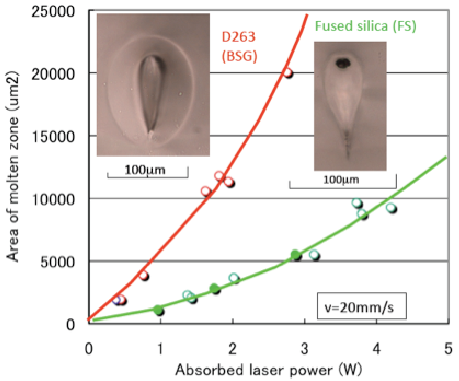

Fig. 2. Cross-sectional area of molten zone plotted vs. absorbed laser power for D263 and fused silica at v=20*mm/s*.

Table 1 Thermal and physical properties of glass

Thermal properties	D263*1)	Fused silica
Density: ρ (g/cm^3)	2.51	2.2
Specific heat: c (J/gK)	0.82	1.1
Thermal diffusivity: α (cm^2/s)	0.003-0.004	0.008
Melting temperature: T_{Melt} (°C)	1,051	2,000
Thermal expansion coefficient	7.2x10^{-6}	5.5x10^{-7}
Band gap energy: E_g (eV)	4.4*2)	9

*1)Schott: Borosilicate glass, *1) Value of Corning 0211

Figure 3(a) shows cross-sections of laser-irradiated fused silica at different translation speeds at a pulse energy of 7.5μJ at a repetition rate of 800kHz using the lens of NA0.55. The shape of the molten region was teardrop at lower translation speeds, and changed into ellipse at higher translation speeds.

3. Laser-matter interaction model

When ultrashort laser pulses are tightly focused into bulk glass with a bandgap larger than the photon energy, free electrons are generated in conduction band through multiphoton ionization. The free electrons subsequently gain kinetic energy from the electric field to produce more free electrons by avalanche ionization, and their energy is transferred to the lattice to provide temperature rise of the bulk glass after the laser pulse. Then the absorbed laser energy is regarded as an instantaneous heat source, since the energy transfer from the electrons to the lattice is much faster than thermal diffusion in the lattice.

The temperature distribution due to Δq instantaneous point heat in the lattice is given by [11]

$$T(x,y,z,t)=\frac{\Delta q}{8c\rho(\pi\omega t)^{3/2}}\exp\left(\frac{r^2}{4\omega t}\right) \tag{2}$$

where c is specific heat, ρ density, α thermal diffusivity, t time after heat generation and $r^2=x^2+y^2+z^2$, assuming c and α are constant. The temperature distribution with arbitrary distribution $q(x,y,z)$ of the absorbed laser energy in fusion welding of glass is given by a spatial and temporal integration of Eq.(2), if $q(x,y,z)$ is known. Several authors evaluated the absorbed laser energy distribution $q(x,y,z)$, when a ultrashort laser pulse is irradiated in the transparent material by solving rate equations for free electrons [12,13]. The procedure is, however, applicable only to a single laser pulse, and the absolute value of $q(x,y,z)$ is difficult to determine.

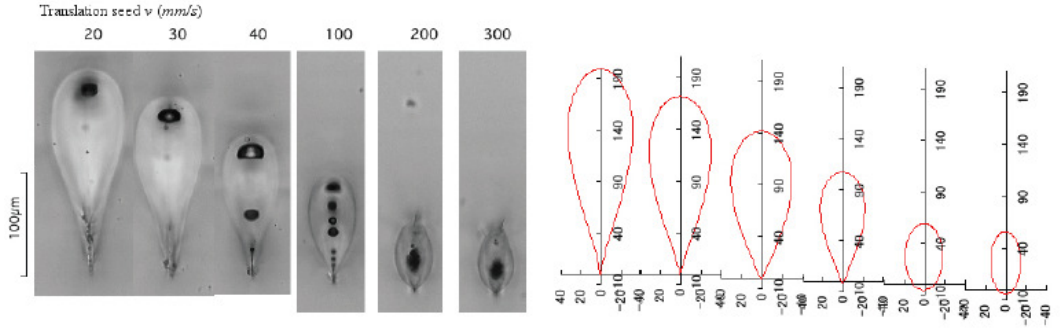

(a) (b)

Fig. 3. (a) Cross-sections of laser-irradiated fused silica at different translation speeds at a pulse energy of Q_0=7.5μJ at a repetition rate of 800kHz. (b) Isothermal line of best fit at 2,000˚C at steady state calculated by **Eq(4).**

In this study, the distribution of absorbed laser energy due to ultrashort laser pulses is evaluated through two steps; first the z-distribution of the absorbed laser energy is evaluated assuming a line heat source model, and second the radial distribution of the absorbed laser energy is determined assuming Gaussian beam propagation [14]. The advantages of our procedure are it can be applicable to successive laser pulses with high repetition rates, and the absolute value is available. An analytical equation to calculate transient temperature distribution is also derived.

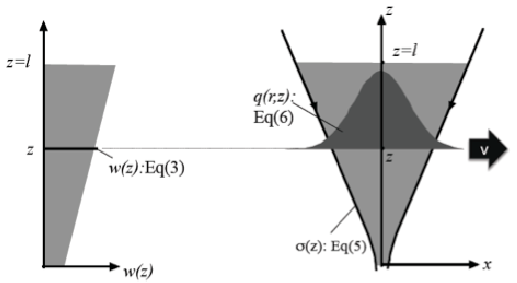

(a) (b)

Fig. 4. (a) Line heat source of continuous power delivery $w(z)$ with a linear function of z given by Eq.(3). (b) Pulse energy of $w(z)/f$ is redistributed into a Gaussian curve with radius $\sigma(z)$ given by Eq.(5), which appears instantaneously at a repetition rate of f.

3.1. Vertical distribution of absorbed laser energy

The temperatures apart from the heat source can be approximated by a line heat source model. As the first attempt, a line heat source with a simple linear function of z with continuous power delivery is assumed;

$$w(z) = az + b - \frac{AW}{l(1+\beta)}\left(\frac{2}{l}z + \beta\right) \tag{3}$$

where l is length of the line heat source, A is nonlinear absorptivity, W is incident laser power and $\beta=2b/(al)$. When the line heat source given by Eq.(3) appears continuously in an infinite solid moving at a constant speed of v in x-direction, the steady temperature $T(x,y,z)$ is given by

$$T(x,y,z) = \frac{AW}{4\pi Kl(1+\beta)}\int_0^l \frac{1}{s}\left\{\frac{2(z-z')}{l}+\beta\right\}\exp\left\{-\frac{v}{2a}(x+s)\right\}dz' \tag{4}$$

where $s^2=x^2+y^2+(z-z')^2$ and K is thermal conductivity. Values of A, l and β in Eq.(4) are determined by fitting the isothermal line of calculated maximum cyclic temperature to the experimental melt contour.

Figure 5 shows the melt isothermal lines corresponding to 2,000°C and distribution of $w(z)$ calculated using physical constants shown in Table 1 at 30mm/s for different values of β. In this calculation, A and l were selected so as to provide the best fit in the length and the width of the molten region, which was found at β=0.3, l=162μm and A=0.66. The isothermal lines of best fit at different translation speeds are shown in Fig. 3(b), showing excellent agreement between the calculated and the experimental melt contours in a wide range of translation speed.

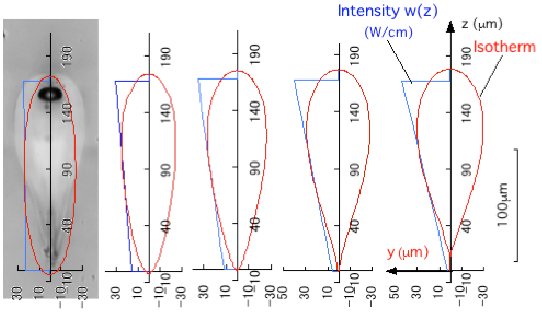

(a) 20 (b) 2.0 (c) 1 (d) 0.3 (e) 0.1

Fig. 5. Fitting of isotheral line of 2,000°C calculated by Eq.(4) to experimental melt contour with different β at v=30mm/s.

Figure 6(a) shows the nonlinear absorptivity A obtained in fitting plotted vs. translation speed. Excellent agreement is found between calculated and experimental results suggesting the validity of our model. The calculated nonlinear absorptivity A increases with increasing v, reaching as high as A=0.85 at v=300mm/s. **Figure 6(b)** shows distribution of $w(z)$ for different translation speeds; $w(z)$ increases with increasing v, indicating the plasma becomes locally more absorbing.

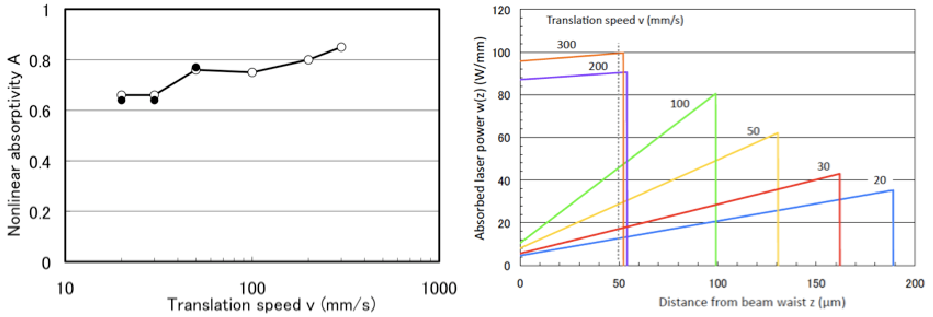

(a) (b)

Fig. 6 (a) Open and closed marks show nonlinear absorptivity of calculated and experimental values at different translation speeds, respectively. (b) Distribution of absorbed laser energy $w(z)$. (β=0.3 at v=20~100mm/s and β=50 at v=200 and 300mm/s)

3.2. Radial distribution of absorbed laser energy density

In our experimental condition of pulse duration 10*ps* and pulse energy 7.5μJ, self-focusing is negligible [15]. So in the second step, it is assumed that the radial distribution of the absorbed laser energy is Gaussian, of which radius is given by

$$\sigma(z) = \eta\omega_0\sqrt{1+\left(\frac{M^2\lambda z}{\pi\omega_0^2 n_g}\right)^2};\quad \omega_0 = \frac{M^2\lambda}{\pi NA}. \tag{5}$$

where M^2 beam quality factor, λ is laser wavelength, n_g is the refractive index of the material and η is a constant (η<1). We also assumed that defocusing due to free electron can be expressed by the effective value of M^2 since the free electron density is especially large near the beam waist, as described latter. Then the intensity of the absorbed laser beam $q(r,z)$ is given by

$$q(r,z) = \frac{2w(z)}{\pi\sigma^2(z)f}\exp\left\{-\frac{2r^2}{\sigma^2(z)}\right\},\quad 0 \le z \le l, \tag{6}$$

where $r^2=x^2+y^2$. The the instantaneous temperature rise $\Delta T(r,z)$ due to $q(r,z)$ is given by

$$\Delta T(r,z) = \frac{q(r,z)}{c\rho} = \frac{2w(z)}{\pi c\rho\eta^2\omega^2(z)f}\exp\left\{-\frac{2r^2}{\eta^2\omega^2(z)}\right\}\ (0 \le z \le l). \tag{7}$$

Assuming that each free electron has mean kinetic energy of $E_g/2$ [12], and that recombination and diffusion loss of free electrons during laser pulse are negligible, the absorbed laser energy per pulse $q(r,z)$ is related with the evolved free electron density $n_e(r,z)$ by

$$q(r,y) = \frac{3}{2}E_g n_g(r,z);(0 \le z \le l) \tag{8}$$

The temperature rise due to the single pulse is directly related to the physical properties of the material by

$$\Delta T(r,z) = \frac{q(r,z)}{c\rho} = \frac{3}{2}\cdot\frac{E_g n_e(r,z)}{c\rho} \tag{9}$$

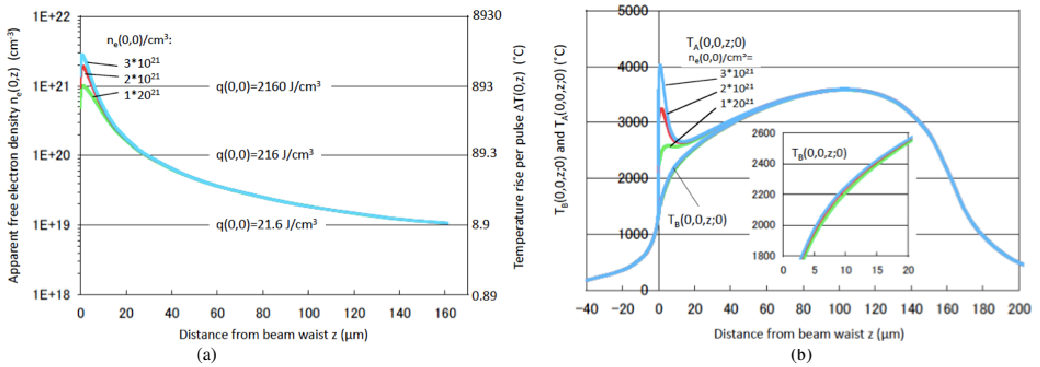

Fig.7. (a) Absorbed laser energy density $q(0,z)$, apparent evolved free electron density $n_e(0,z)$ and temperature rise per pulse $\Delta T(0,z)$. (b) Distribution of $T_B(0,0,z;0)$, $T_A(0,0,z;0)$ and $\Delta T(0,z)$ (Fused silica, v=30*mm/s*, f=800kHz, Q_0=7.5μJ, NA0.55, η=0.6).

The densities of the absorbed laser energy $q(0,z)$ and the corresponding evolved free electron $n_e(0,z)$ for 30*mm/s* in fused silica are plotted for different values of $n_e(0,0)$ in **Fig. 7(a)**. Assuming that $n_e(0,0)$ is equal to or lower than the critical density of $10^{21}/cm^3$ at the wavelength of λ=1.06μm, the temperature rise per pulse at the beam waist $\Delta T(0,0)$ is lower than 893˚*C* in fused silica, and 513˚C in D263. As seen in Table 1, these values are significantly lower than the melting temperature of 2,000˚*C* and 1,053˚*C* in fused silica and D263, respectively. This contradicts

the fact that the glass can be melted by single laser pulse [5], suggesting that $n_e(0,0)$ can exceed $10^{21}/cm^3$ in spite of that the plasma becomes highly reflective at such a high free electron density.

Free electron loss by recombination and diffusion during laser pulse can account for the contradiction. This means that $n_e(0,0)$ in Eq.(9) is an apparent free electron density, and consists of the actual free electron density plus the lost free electron density. Thus one can evaluate the actual free electron density by subtracting the free electron density lost by the recombination and the diffusion from Eq.(9), and the actual free electron density is expected to be $\approx 10^{21}/cm^3$. Such a high free electron density evaluated at the beam waist is supported by the fact that the glass sample is melted only in the cone angle of the laser beam proximal to the laser, indicating the region beyond the beam waist is shielded by the strong absorption there, as seen in Fig. 3. The effect of the recombination losses is especially large near the beam waist, since the recombination loss is proportional to n_e^2.

In Fig. 7(a), the temperature rise per pulse $\Delta T(0,z)$ is plotted for apparent free electron density of $n_e(0,0)=10^{21}/cm^3$, $2*10^{21}/cm^3$ and $3*10^{21}/cm^3$, respectively, and $\Delta T(0,z)$ reaches the melting temperature at $\approx 2.2*10^{21}/cm^3$. This suggests that apparent free electron density is $n_e(0,0)\approx 2.2*10^{21}/cm^3$ or higher. Further study is, however, needed for quantitative evaluation the recombination loss near the beam waist. It is noted that the assumption of the instantaneous heat source is still valid, since the energy produced on recombination or diffusion is eventually transferred into heat to elevate the lattice temperature in a time much shorter than thermal diffusion.

The absorbed laser energy density $q(0,z)$ and the instantaneous temperature rise $\Delta T(0,z)$ in the plasma column decrease rapidly with increasing z; $\Delta T(0,l)$ is as small as less than $10\,^{\circ}C$, which is approximately two order smaller than $\Delta T(0,l)$.

3.3. Transient temperature distribution in plasma column

A thermal conduction equation due to the instantaneous heat source $q(r,z)$ given by Eq.(6), have been derived, which appears at a repetition rate of f in an infinite solid moving at a constant speed v along x-axis as schematically shown in Fig. 4(b). The transient temperature rise $T(x,y,z;t)$ at (x,y,z) at time t after generation of N-th pulse is written in a form

$$T(x,y,z;t)=\frac{1}{\pi c\rho f}\sum_{i=0}^{N-1}\frac{1}{\sqrt{\pi\alpha\left(t+if^{-1}\right)}}\int_0^{l}\frac{w(z')}{\eta^2\omega^2(z')+8\alpha\left(t+if^{-1}\right)}\exp\left[-\frac{2\left\{\left(x+v\left(t+if^{-1}\right)\right)^2+y^2\right\}}{\eta^2\omega^2(z')+8\alpha\left(t+if^{-1}\right)}-\frac{(z-z')^2}{4\alpha t}\right]dz'. \tag{10}$$

The temperature $T_B(0,0,z;0)$ and $T_A(0,0,z;0)$ at steady state of $N\rightarrow\infty$ are plotted in Fig. 7(b). It is seen that $T_A(0,0,z;0)$ at $z\approx 0$ reaches approximately 2500°C, 3200°C and 4000°C at $n_e(0,0)$ of $10^{21}/cm^3$, $2*10^{21}/cm^3$ and $3*10^{21}/cm^3$, respectively. On the other hand, the effect of $n_e(0,0)$ on $T_B(0,0,z;0)$ is very small, since the local temperature rise is diffused out due to high cooling rate. It is noted that $T_B(0,0,;0)$ decreases down to as low as approximately $1{,}300\,^{\circ}C$, suggesting that the material at the beam waist is cooled down lower than melting temperature at time just before pulse impingement.

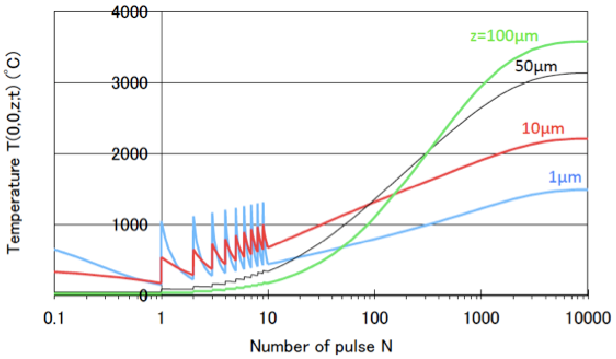

Fig. 8 Temperature change at $(0,0,z)$ in fused silica calculated at v=30mm/s, f=800kHz, Q_0=7.5μJ and NA0.55.

Figure 8 shows the change in temperature T(*0,0,z;t*) in each pulse is plotted in logarithmic time scale until pulse number of *N*=10 in fused silica at 30*mm/s*, assuming the apparent free electron density of $n_e(0,0,0)=10^{21}/cm^3$, and at *N*>10 only $T_B(0,0,z;0)$ is plotted for clear picture. As *z* approaches zero, the amplitude of the temperature change becomes largest since the absorbed laser energy density is largest. Extremely high cooling rate is evaluated higher than 10^6°*C/s*, due to large temperature gradient caused by small spot size and small heat accumulation.

It is seen that the base temperature $T_B(0,0,z;0)$ increases as *N* increases due to heat accumulation, and steady temperature is not reached until *N*≈5,000. The heat accumulation is strongly dependent on *z*; as *z* increases, the heat accumulation becomes significant due to increase in the laser spot size, leading to higher steady temperature, although the temperature rise per pulse diminishes. Highest steady temperature is reached at *z*≈100μm, whereas the temperature rise per pulse is as small as ≈9°C.

The laser spot radius at z_m=100μm at 30*mm/s* is as large as approximately 40μm, at which laser intensity is much lower than the breakdown threshold of the multiphoton ionization [10,16]. A simple calculation indicates that $T_B(0,0,z_m;0)$≈3,500°*C* provides the thermally excited electron density of the order of $10^{10}/cm^3$ to the conduction band in fused silica (E_g=9*eV*). This free electron density is large enough for seeding avalanche ionization, suggesting that the laser energy is absorbed by the inverse bremsstrahlung. In contrast, the temperature at the beam waist is as low as $T_B(0,0,0;0)$≈1,330°*C*, providing negligible free electrons in the focus volume by the thermal excitation. This suggests that the seed free electrons for avalanche ionization are provided solely by multiphoton ionization at the beam waist.

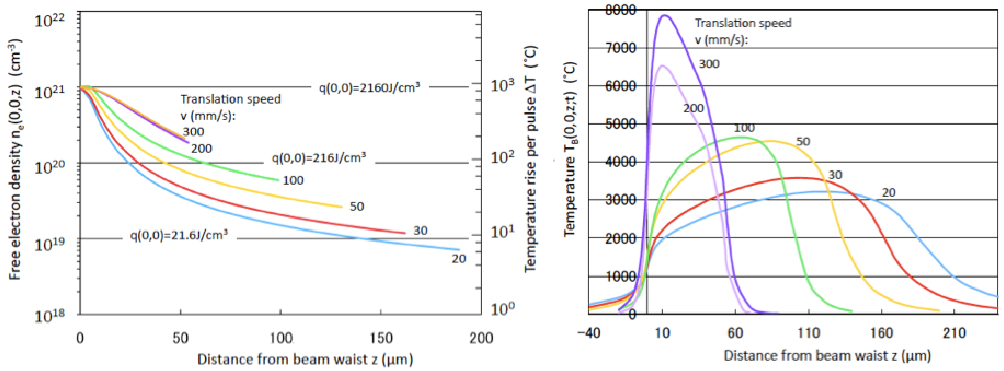

(a) (b)

Fig. 9. (a) Distribution of evolved free electron density $n_e(0,0,z)$, absorbed laser energy density q(0,0,z) and instantaneous temperature rise per pulse ΔT(0,0,z). assuming apparent free electron density of $n_e(0,0)=10^{21}/cm^3$. (b) Temperature distribution just before laser pulse $T_B(00,z;0)$. (f=800kHz, Q_0=7.5μJ, NA0.55, η=0.6)

3.4. Effect of translation speed

The distribution of the apparent free electron density $n_e(0,z)$ and the temperature distribution just before the laser pulse $T_B(0,0,z;0)$ were calculated, assuming that the apparent free electron density evolved at the center of the beam waist reaches n_{cr}. **Figure 9** shows the apparent free electron density $n_e(0,z)$ and the temperature just before the laser pulse $T_B(0,0,z;0)$ calculated at different translation speeds and the corresponding distributions of the free electron density $n_e(0,0,z)$ evolved in the plasma column. It is seen that the maximum value of $T_B(0,0,z:0)$ increases with increasing translation speeds, ranging ≈3,200°*C* at 20*mm/s* to ≈7,800°*C* at 300*mm/s*, suggesting more free electrons are thermally excited to the conduction band. This agrees with the aforementioned higher nonlinear absorptivity and higher absorption coefficient shown in Fig. 6. These results suggest that the seed free electrons for avalanche ionization can be provided by thermal excitation without multiphoton ionization at least at locations apart from the beam waist.

4. Properties of laser-welded joint

4.1. Effect of heat shock on cracking

Crack tendency can be qualitatively evaluated from $T_B(0,0,z;0)$ and ΔT, although quantitative evaluation of stress field during welding needs numerical elasto-plasticity analysis; $T_B(0,0,z;0)$ and ΔT are measures of ductility of material at the pulse impingement and the thermal shock, respectively.

Figure 10(a) shows $T_B(0,0,z;0)$ and $\Delta T(0,0,z)$ calculated at 30*mm/s* for D263. **Figure 10(b)** shows the relation ship between $T_B(0,0,z;0)$ and $\Delta T(0,0,z)$ for fused silica and D263. It is seen that large thermal load in applied near the bottom tip of the teardrop-shaped region in fused silica when it is at low temperature having low ductility, resulting cracking shown in Fig. 3. In D263, on the other hand, the largest thermal load is applied at temperatures higher than melting temperature, so that no crack occurs. In spite of the fact that fused silica has much lower thermal expansion coefficient than D263, the crack tendency of fused silica is higher than D263. This is caused by its large thermal diffusivity and melting temperature.

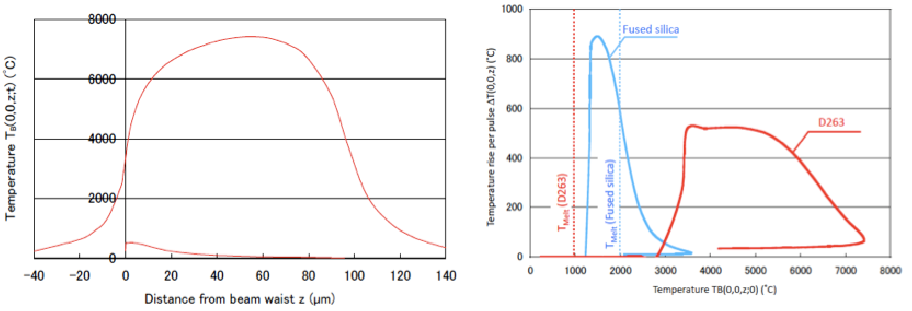

(a) (b)

Fig. 10. (a) $T_B(0,0,z;0)$ and $\Delta T(0,0,z)$ calculated at 20*mm/s* for D263. (b) Relationship between $T_B(0,0,z;0)$ and $\Delta T(0,0, z)$ in fused silica (Fig. 7b) and D263 (Fig. 10a). (f=800kHz, Q=7.5μJ, NA0.55)

4.2. Mechanical strength of weld joint

In fusion welding of glass with ultrashort laser pulses, optical contact is needed between glass plates in order to keep the high-temperature plasma in the bulk glass. **Figure 11(a)** shows the appearance of weld joint cleaved after cooling. It is seen that the original flat interface disappears indicating two glass plates coalesces by melting. As shown in **Fig. 11(b)**, the cross-section of multi-path weld joint is also accomplished without crack-development, indicating the fusion procedure technology by ultrashort laser pulse is very versatile.

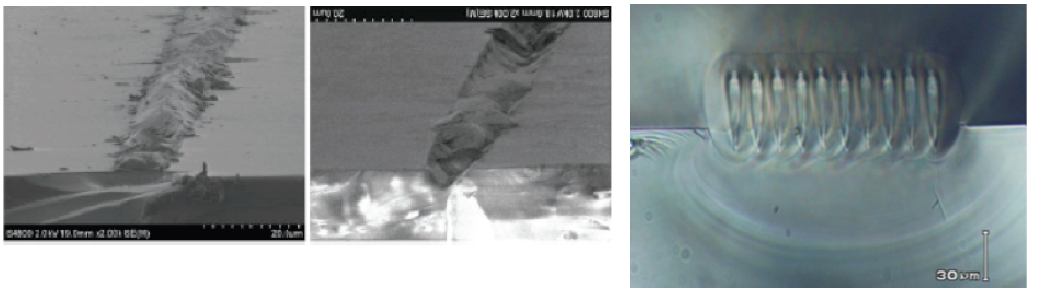

(a) (b)

Fig. 11. (a) Appearance of overlap weld joint, which was pealed-off at the interface. (b) An example of multipath welding. The interface line disappears in the outer elliptical region where the transmission changes indicating molten region. (Material: D263)

The mechanical strength of the weld joint was evaluated by applying the shear stress to the overlap weld joint. Different number of weld bead n was produced with the optical contact area of S_{OPT}=10*mm*x35*mm* at a translation speed of 20*mm/s*. **Figure 12** shows the rupture strength in the mechanical test obtained for different numbers of weld bead of n=0, n =1, n =3 and n =10. It is noted that large rupture strength was measured without weld bead due to the optical contact force caused by the attracting force between two plates. The optical contact strength P_{OC}=F_{OC}/S_{OPT} is evaluated to be approximately 0.25*MPa* from n=*0*. The shear strength of the weld joint is obtained by subtracting the optical contact force F_{OC} from the rupture force F_{RUP} at given value of n by (F_{RUP}-F_{OC})/S_{BEAD}. The shear strength of the weld joint with n=1 is thus evaluated to be ≈55MPa, which is approximately 200 times larger than the optical contact force. It should be noted, however, the optical contact force can exceed the weld joint. As the number of the weld bead increases, the shear strength of the weld joint is seen to decrease. This is considered to be because non-uniform stress of applied to each weld bead or residual stress.

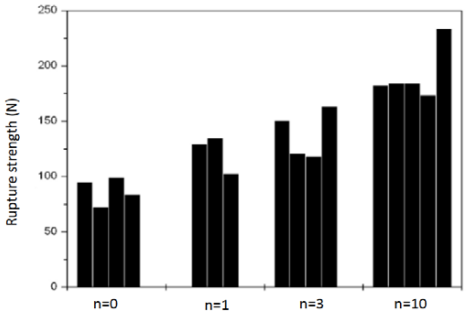

Fig. 12. Mechanical test results for samples of overlap-joint and internal melting at 20*mm/s* in D263. Rupture load of overlap-joint is plotted at different numbers of weld bead (weld area S_{Weld}=0.62mm^2, optical contact area S_{Opt}=350mm^2.

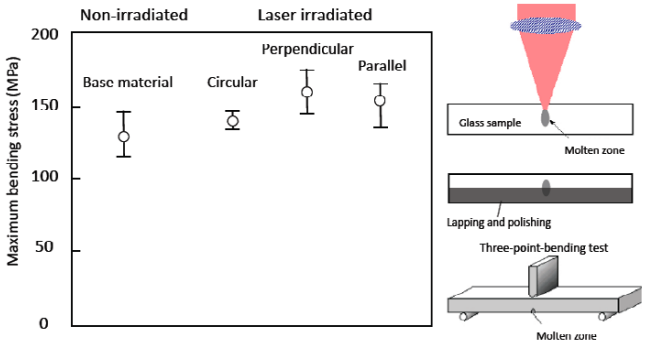

Fig. 13 Maximum bending stress of internally melted zone with different polarizations with respect to translation direction. Three-point-bending test was performed with applying maximum stress at the molten zone.

In order to evaluate the mechanical strength of the molten zone without the influence of joint geometry, bulk glass was internally melted by irradiating the focused laser beam in the bulk glass, and the surface layer was removed by lapping and polishing to expose the molten zone to the surface. Then a three-point-bending test was performed to apply the maximum bending stress to the molten region as shown in **Fig.13**. In this experiment, the effect of polarization vector of the laser beam with respect to the translation direction of the sample was also examined to examine the effect of nano-grating, which can be produced perpendicularly to the polarization vector [17]. It was found that the mechanical strength of the laser-irradiated samples was approximately 150MPa, which is even higher than that of the base material presumably due to compressive residual stress produced in the laser-irradiated region. The result also shows that the effect of polarization on mechanical strength is negligible.

5. Summary

A novel fusion welding technology of glass using ultrashort laser pulses with duration of 10*ps* has been developed, where the laser energy is absorbed by nonlinear process to melt the interface selectively without pre- and post-heating. The nonlinear absorptivity at given pulse energy increases with increasing pulse repetition rate. A laser-matter interaction model has been developed, by which the absorbed energy density distribution of the ultrashort laser pulses in fusion welding of glass was evaluated at high repetition rates. Thermal conduction equation is derived to calculate transient 3-dimensional temperature distribution during welding process. The model indicates that higher nonlinear absorptivity at higher pulse repetition rates is attributed to the effect of the thermally excited free electrons.

The mechanical strength of weld joint is evaluated taking into consideration of the attracting force of the optical contact between the glass plates for keeping the high-temperature plasma in the bulk glass. The mechanical strength of molten region as high as that of base material was obtained, and the shear strength of overlap joint was higher than 50*MPa*.

Acknowledgements

This work was partially supported by Erlangen Graduate School in Advanced Optical Technologies (SAOT).

References

1. Y. Arata, H. Maruo, I. Miyamoto, S. Takeuchi, *Proc. 7th Int. Conf. on Electron and Ion beam Science and Technology* (1978) 111.
2. T. Tamaki, W. Watanabe, J. Nishii, K. Itoh, Japanese J. Appl. Phys. **44**, (2005) L687
3. I. Miyamoto, A. Horn, J. Gottmann, D. Wortmann, F. Yoshino, J. Laser Micro/Nanoengineering, **2** (2007) 57.
4. A. Horn, I. Mingareev, Werth, Kachel, Brenk, Appl. Phys. A, **93** (2008) 171.
5. I. Miyamoto, A. Horn, J. Gottmann, J. Laser Micro/Nanoengineering, **2** (2007) 7
6. C.M. Warwick, M. Gordon, Proc, Joining Plastics (2006) 25
7. I. Miyamoto, T. Herrmann, *Proc. 8th International Symposium on Laser Precision Microfabrication*, (2007) #07-25
8. W. Watanabe, S. Onda, T. Tamaki, K. Itoh, J. Nishii, Appl. Phys. Lett, **89**, (2006) 021106 1-3
9. T. Tamaki, W. Watanabe, K. Itoh, Optics Express, **14**, (2006) 10468
10. K. Nahen, A. Vogel, IEEE J. Selected Topics in Quantum Electronics, **2** (1996) 861
11. H.S. Carsloaw, J.C. Jaeger: "Conduction of heat in solids", 353 (Oxford at the Clarendon Press, 1959).
12. J. Noack, A. Voge, IEEEJ. Quantum Electronics, **35** (1999) 1156
13. C.L. Arnold, A. Heisterkamp, W. Ertmer, H. Lubatschowski, Optics Express,**15**, (2007) 10303
14. A.E. Stiegman, S.W. Townsent, IEEE J. Quant. Elect., **29** (1993) 1212
15. M.J. Soileau, W.E. Williams, N. Mansour, E.W. Stryland, Opt. Eng, 28 (1989) 1133
16. C.B. Schaffer, A. Brodeur, E. Mazur, Meas. Sci. Technol, **12**, (2001) 1784
17. C. Hnatovsky, R.S. Taylor, Appl. Phys. Lett., **87** (2005) 014104